PERGAMON

International Journal of Heat and Mass Transfer 41 (1998) 3213–3227

International Journal of HEAT and MASS TRANSFER

Heat and fluid flow in pulsed current GTA weld pool

W.-H. Kim*, S.-J. Na

Agency for Defense Development of Korea Yuseong P.O. Box 35 (4-4-2), Taejon, 305-600 Korea

Received 4 September 1997; in final form 9 January 1998

Abstract

In this study the heat transfer, fluid flow and phase change of the weld pool in pulsed current gas tungsten arc (GTA) welding were investigated. Transporting phenomena from the welding arc to the base material surface, such as current density, heat flux, arc pressure and shear stress acting on the weld pool surface, were taken from the simulation results of the corresponding welding arc.

Various driving forces for the weld pool convection were considered, namely self-induced electromagnetic, surface tension, buoyancy, and impinging plasma arc force. Furthermore, the effect of deformed free surface due to the arc pressure acting on the weld pool surface was considered.

Heat and mass transfer equations, including the generalized Navier–Stokes equation and electric transport equation, were solved by a finite difference method.

Because the fusion boundary has a curved and unknown shape during welding, a boundary-fitted coordinate system was adopted to precisely describe the boundary for the momentum equation. The numerical model for pulsed current welding was applied to AISI 304 stainless steel and compared with the results of the constant current.

Nomenclature

a_i activity of species i in solution, weight %
A_γ constant in surface tension gradient, N (m K)$^{-1}$
B_θ θ-directional self-induced magnetic flux density, Wb m^{-2}
C_p specific heat at constant pressure, J (kg K)$^{-1}$
F_p pulse cycle frequency, Hz
f_L fraction of molten metal
ΔH latent heat of fusion, J kg^{-1}
ΔHo standard heat of adsorption, J (kg mole)$^{-1}$
h_c combined heat transfer coefficient at body surface, W (m^2 K)$^{-1}$
I welding current, A
I_B background current, A
I_E effective current, A
I_M mean current, A
I_P peak pulse current, A
J (j_r, j_z), current density vector, A m^{-2}
j current density distribution at surface, A m^{-2}
j_r r-directional current density component, A m^{-2}
j_z z-directional current density component, A m^{-2}
k thermal conductivity, W (m K)$^{-1}$
k_1 constant related to entropy of segregation, 3.18×10^{-3}
m total number of iteration
n normal direction to surface
P_{arc} arc pressure acting on base plate, Pa
R_g gas constant, J (kg mole K)$^{-1}$
r_0 radius of weld pool surface, m
r_E current ratio
r_1 peak to total time ratio
T temperature, K
T_L liquidus temperature, K
T_r reference temperature, K
T_s solidus temperature, K
t_B background duration, s
t_P peak pulse duration, s
t_R pulse time ratio, t_P/t_B
t_T total time, $t_B + t_P$, s
u r-directional velocity component, m s^{-1}
w z-directional velocity component, m s^{-1}.

Greek symbols

β coefficient of thermal expansion, K^{-1}
γ surface tension, N m^{-1}

* Corresponding author.

0017–9310/98 $19.00
PII: S0017-9310(98)00052-0

γ_m surface tension at melting point, N m^{-1}
$d\gamma/dT$ surface tension gradient, N (m K)$^{-1}$
Γ_s surface excess at saturation, J (kg mole m^2)$^{-1}$
Γ_Φ general diffusion coefficient
ε emissivity of body surface
λ_L Lagrange multiplier
μ dynamic viscosity, kg (m s)$^{-1}$
μ_o magnetic permeability of vacuum, H m^{-1}
ξ, ζ transformed coordinate system
ρ density, kg m^{-3}
σ electrical conductivity, 1 (Ω m)$^{-1}$
τ_a shear stress acting on base plate, N mm^{-2}
ϕ electrical potential, V.

1. Introduction

It is well known that the heat transfer experienced by the weldment during welding can alter the microstructure and thus the properties of the weldment. Therefore the heat transfer and fluid flow in the weld pool can significantly influence such factors as the weld pool geometry, the temperature gradients, the local cooling rates and the solidification structure. In recent years, there have been a increased effort to develop mathematical models to describe the phenomena occuring during welding process, the ultimate goal of this investigations being to determine how the process parameters affect weldment quality [1].

Pulsed current gas tungsten arc welding (GTAW) is a relatively new welding process that has been reported to have numerous advantages over the conventional GTA process. The beneficial effects most often reported in the literature include claims that the total heat input to the weld is reduced, which results in the reduction of weld bead size, residual stresses, distortion, and porosity [2].

An experimental study of pulsed current GTA welding was conducted to determine the effects of frequency on the arc column and weld pool by Saedi et al. [3]. Recently, Vishnu et al. [4] conducted an analytical model of the heat flow during pulsed welding. But, until now no attempt has been made to completely evaluate the pulsed current GTA welding mode by suing a numerical model.

The main driving forces for weld pool circulation have been identified as electromagnetic, surface tension, buoyancy, and impinging plasma arc force. Of the four forces, the first two or three have been treated very extensively in the literature because they can be calculated quite independently of the welding arc [1, 5]. But, in order to consider the impinging plasma arc force, the welding arc must be simulated to obtain a gas shear over the free surface, because the role that the gas drag force plays at the surface is quite complex. In addition, only recently the coupling of the constant welding arc with the weld pool has been carried out [6, 7].

In this work, numerical analysis of heat, fluid flow and phase change in a pulsed current GTA welding pool were conducted by considering the above four forces. Heat and mass transfer equations, including the generalized Navier–Stokes equation and electric transport equation, were solved by a finite difference model. Because the fusion boundary has a curved and unknown shape during welding, a boundary-fitted coordinate system was adopted to precisely describe the boundary for the momentum equation. The transporting phenomena from the welding arc to the base material surface, such as current density, heat flux, arc pressure and gas shear stress acting on the weld pool surface, were taken from the simulation results of the corresponding welding arc.

The numerical model was applied to AISI 304 stainless steel and compared with the constant current results. Particularly, the change of weld bead shape, velocity distribution, temperature distribution, and stream function contours were determined and discussed. This numerical analysis should be helpful in establishing the initial parameters used in the development of pulsed current GTA welding procedures.

2. Computational model

Figure 1 shows a schematic representation of the stationary GTA (gas tungsten arc) weld pool with DCSP (direct current straight polarity), together with each driving force, geometry and coordinate system of the computational weld zone to be used in the following calculations. The r- and z-component of flow velocities are represented by u and w, respectively.

A computational model using a finite difference analysis was appropriately modified to investigate the transient, two-dimensional heat and fluid flow problem associated with the pulsed current GTA welding process. To analyze the weld pool convection, the following driving forces were considered:

(1) Electromagnetic or Lorentz force generated by the action of current density on the induced magnetic field;
(2) Surface tension or Marangoni force due to the temperature gradient;
(3) Impinging plasma arc force or gas drag force on the surface of the weld pool due to the plasma jet momentum;
(4) Buoyancy force due to changes in temperature of the weld pool.

In formulating the model, the following major assumptions have been made:

(1) The flow is laminar and incompressible [1, 6, 7];
(2) The system is axisymmetric;
(3) The pulsed heat source is a square wave form;

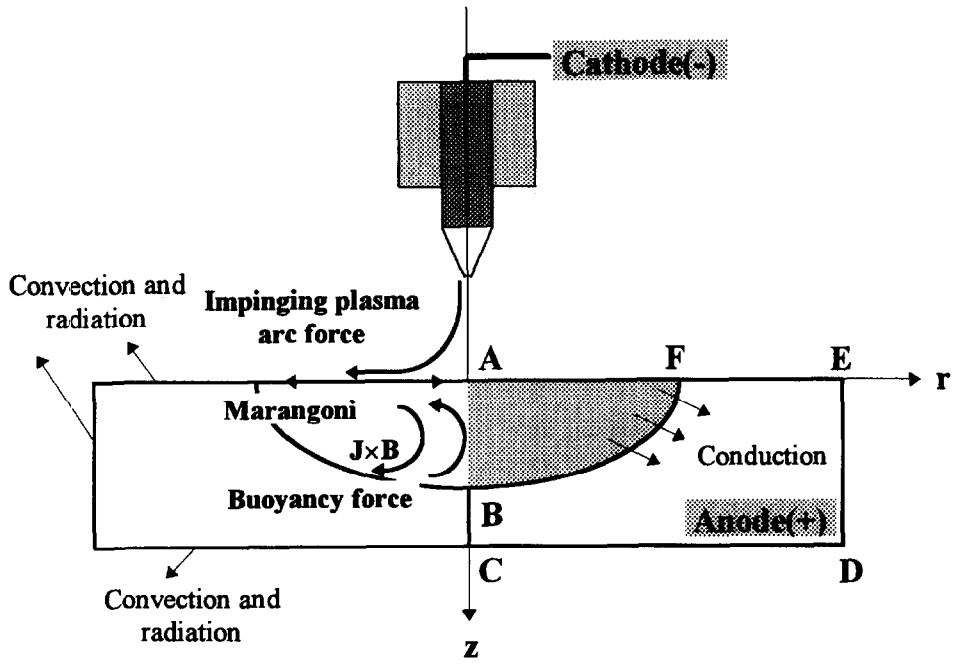

Fig. 1. Schematic representation of GTA welding pool with driving forces.

(4) The arc pressure was only responsible for the surface depression of the weld pool;
(5) The material properties are independent of temperature (except for the temperature-dependent surface tension, specific heat and thermal conductivity). Boussinesq approximation is used [1];
(6) The heat and current density distributions were obtained by the simulated results, which were calculated under the assumption of a steady state welding arc. It was also assumed that the electrical potential of the base plate did not vary with time.

2.1. Governing equations

With the above assumptions, the Navier–Stokes equations for the weld pool may be written as follows:

(1) Conservation of mass

$$\frac{1}{r}\frac{\partial}{\partial r}(\rho r u)+\frac{\partial}{\partial z}(\rho w)=0 \tag{1}$$

(2) Conservation of radial momentum

$$\frac{\partial}{\partial t}(\rho u)+\frac{u}{r}\frac{\partial}{\partial r}(\rho r u)-\frac{2}{r}\frac{\partial}{\partial r}\left(\mu r\frac{\partial u}{\partial r}\right)+w\frac{\partial}{\partial z}(\rho u)-\frac{\partial}{\partial z}\left[\mu\left\{\frac{\partial w}{\partial r}+\frac{\partial u}{\partial z}\right\}\right]=-\frac{\partial p}{\partial r}-2\mu\frac{u}{r^2}-j_z B_\theta \tag{2}$$

(3) Conservation of axial momentum

$$\frac{\partial}{\partial t}(\rho w)+w\frac{\partial}{\partial z}(\rho w)-2\frac{\partial}{\partial z}\left(\mu\frac{\partial w}{\partial z}\right)+\frac{u}{r}\frac{\partial}{\partial r}(\rho r w)-\frac{1}{r}\frac{\partial}{\partial r}\left[\mu r\left\{\frac{\partial u}{\partial z}+\frac{\partial w}{\partial r}\right\}\right]=-\frac{\partial p}{\partial z}+j_r B_\theta-\rho g\beta(T-T_r) \tag{3}$$

(4) Conservation of thermal energy

$$\frac{\partial}{\partial t}(\rho C_p T)+\frac{u}{r}\frac{\partial}{\partial r}(\rho C_p r T)+w\frac{\partial}{\partial z}(\rho C_p T)=\frac{1}{r}\frac{\partial}{\partial r}\left(kr\frac{\partial T}{\partial r}\right)+\frac{\partial}{\partial z}\left(k\frac{\partial T}{\partial z}\right)-\frac{\Delta H}{C_p}\frac{\partial f_L}{\partial t} \tag{4}$$

(5) Conservation of electrical charge

$$\frac{1}{r}\frac{\partial}{\partial r}\left(\sigma r\frac{\partial\phi}{\partial r}\right)+\frac{\partial}{\partial z}\left(\sigma\frac{\partial\phi}{\partial z}\right)=0 \tag{5}$$

The current density can be obtained from the definition of electric potential as follows.

$$J=-\sigma\nabla\phi$$

$$j_r=-\sigma\frac{\partial\phi}{\partial r},\quad j_z=\sigma\frac{\partial\phi}{\partial z} \tag{6}$$

Since the current distribution is axisymmetrical, the self-induced azimuthal magnetic field is derived from Ampere's law as follows.

$$B_\theta = \frac{\mu_0}{r}\int_0^r j_z r\,\mathrm{d}r \tag{7}$$

The latent term is added to the conservations of thermal energy where f_L, the fraction of liquid, has been linearized for simplicity. It can be sued to simulate the true liquid volume fraction if the phase diagram of the alloy is known. Here, it is given as:

$$T > T_L \quad f_L = 1$$

$$T_S \leqslant T \leqslant T_L \quad f_L = \frac{T-T_S}{T_L-T_S}$$

$$T < T_S \quad f_L = 0 \tag{8}$$

Two other driving forces, the surface tension and impinging plasma arc forces, are added as boundary conditions.

2.2. Boundary conditions

The boundary conditions are shown in Table 1, for which A to F are represented in Fig. 1. At the free surface (region AF), the surface tension or Marangoni-driven flow is described by

$$-\mu\frac{\partial V_s}{\partial n} = \tau_a + \frac{\mathrm{d}\gamma}{\mathrm{d}T}\frac{\partial T}{\partial s}. \tag{9}$$

In this study, the following relationship between surface tension and temperature was used [8, 9]:

$$\gamma(T) = \gamma_m - A_\gamma(T-T_m) - R_g T\Gamma_s \ln(1+Ka_i) \tag{10}$$

where

$$K = k_1 \exp\left(-\frac{\Delta H_0}{R_g T}\right) \tag{11}$$

The temperature-dependent surface tension gradient for alloys with a surface-active element was obtained by differentiating equation (10) with respect to T as follows:

$$\frac{\mathrm{d}\gamma}{\mathrm{d}T} = -A_\gamma - R_g\Gamma_s \ln(1+Ka_i) - \frac{Ka_i}{(1+Ka_i)}\frac{\Gamma_s\Delta H_0}{T} \tag{12}$$

The heat transfer boundary conditions in region CD, DE and EF are used as in the following equation.

$$h_c(T-T_\infty) = -k\frac{\partial T}{\partial z} \tag{13}$$

where h_c is a combined heat transfer coefficient for the radiative and convective boundary conditions. The h_c can be calculated from the relationship given by Goldak *et al.* [10].

$$h_c = 24.1\times10^{-4}\varepsilon T^{1.61}\,[\mathrm{W\,(m^2\,^\circ C)^{-1}}] \tag{14}$$

where ε is the emissivity of the body surface. A value of 0.9 was assumed for ε, as recommended for hot rolled steels [11].

2.3. Surface deformation

The weld pool is distorted by the arc pressure and gravitational force. The surface tension acts to support the weld pool for the arc–pool interface, i.e., the top pool surface and the static force balance can be described as follows [12].

Table 1
Boundary conditions for weld pool model

	u	w	T	Φ
AB	0	$\frac{\partial w}{\partial r}=0$	$\frac{\partial T}{\partial r}=0$	$\frac{\partial \phi}{\partial r}=0$
BC	0	0	$\frac{\partial T}{\partial r}=0$	$\frac{\partial \phi}{\partial r}=0$
CD	0	0	$h_c(T-T_\infty) = -k\frac{\partial T}{\partial z}$	$\frac{\partial \phi}{\partial z}=0$
DE	0	0	$h_c(T-T_\infty) = -k\frac{\partial T}{\partial r}$	$\frac{\partial \phi}{\partial r}=0$
EF	0	0	$q_n(r) = -k\frac{\partial T}{\partial n}$	$j_n(r) = -\sigma\frac{\partial \phi}{\partial n}$
FA	$-\mu\frac{\partial V_S}{\partial n} = \tau_a + \frac{\mathrm{d}\gamma}{\mathrm{d}T}\frac{\partial T}{\partial s}$	0	$q_n(r) = -k\frac{\partial T}{\partial n}$	$j_n(r) = -\sigma\frac{\partial \phi}{\partial n}$

$$\gamma\left\{\frac{rz_{rr}+z_r(1+z_r^2)}{r(1+z_r^2)^{\frac{2}{3}}}\right\} = \rho g z - P_{arc} + \lambda_L \tag{15}$$

where

$$z_r = \frac{\partial z}{\partial r}$$

$$z_{rr} = \frac{\partial^2 z}{\partial r^2} \tag{16}$$

In the computational procedure, the iterative method of finite difference has been used to solve this nonlinear differential equation. If it does not satisfy the constraining equation, the computation is repeated after modification of the Lagrange multiplier λ in equations (15).

3. Procedure of numerical analysis

3.1. Transformation of governing equations

The governing equations (1)–(5) are transformed to a general curvilinear coordinate system (ξ, ζ), which results in equation (17).

$$\frac{\partial U}{\partial t} + \frac{1}{r}\left(\frac{\partial E}{\partial \xi}\frac{\partial \xi}{\partial r} + \frac{\partial E}{\partial \zeta}\frac{\partial \zeta}{\partial r}\right) + \left(\frac{\partial G}{\partial \xi}\frac{\partial \xi}{\partial z} + \frac{\partial G}{\partial \zeta}\frac{\partial \zeta}{\partial z}\right) = S \tag{17}$$

where

$$\frac{\partial \xi}{\partial r} = \frac{1}{J}\frac{\partial z}{\partial \zeta}, \quad \frac{\partial \zeta}{\partial r} = -\frac{1}{J}\frac{\partial z}{\partial \xi}, \frac{\partial \xi}{\partial z} = -\frac{1}{J}\frac{\partial r}{\partial \zeta},$$

$$\frac{\partial \zeta}{\partial z} = \frac{1}{J}\frac{\partial r}{\partial \xi}, \quad J = \frac{\partial r}{\partial \xi}\frac{\partial z}{\partial \zeta} - \frac{\partial r}{\partial \zeta}\frac{\partial z}{\partial \xi} \tag{18}$$

The transformation coefficients,

$$\frac{\partial \xi}{\partial r}, \frac{\partial \zeta}{\partial r}, \frac{\partial \xi}{\partial z}, \frac{\partial \zeta}{\partial z}, \frac{\partial r}{\partial \xi}, \frac{\partial r}{\partial \zeta}, \frac{\partial z}{\partial \xi}, \frac{\partial z}{\partial \zeta}$$

are computed numerically using the second order central differencing. In the transformed domain, the grid size (i.e. $\Delta\xi$, $\Delta\zeta$) are set at unity, which simplifies the calculation of transformation coefficients.

Equation (17) can be represented by the following model transport equation in which Φ denotes all the dependent variables and Γ the diffusion coefficient.

$$\frac{\partial}{\partial t}(\rho\Phi) + \frac{1}{r}\frac{\partial}{\partial \xi}\left[r\left\{\rho u\Phi - \Gamma_\Phi\left(\frac{\partial \Phi}{\partial \xi}\frac{\partial \xi}{\partial r} + \frac{\partial \Phi}{\partial \zeta}\frac{\partial \zeta}{\partial r}\right)\right\}\right]\frac{\partial \xi}{\partial r}$$

$$+ \frac{1}{r}\frac{\partial}{\partial \zeta}\left[r\left\{\rho u\Phi - \Gamma_\Phi\left(\frac{\partial \Phi}{\partial \xi}\frac{\partial \xi}{\partial r} + \frac{\partial \Phi}{\partial \zeta}\frac{\partial \zeta}{\partial r}\right)\right\}\right]\frac{\partial \zeta}{\partial r}$$

$$+ \frac{\partial}{\partial \xi}\left\{\rho w\Phi - \Gamma_\Phi\left(\frac{\partial \Phi}{\partial \xi}\frac{\partial \xi}{\partial z} + \frac{\partial \Phi}{\partial \zeta}\frac{\partial \zeta}{\partial z}\right)\right\}\frac{\partial \xi}{\partial z}$$

$$+ \frac{\partial}{\partial \xi}\left\{\rho w\Phi - \Gamma_\Phi\left(\frac{\partial \Phi}{\partial \xi}\frac{\partial \xi}{\partial z} + \frac{\partial \Phi}{\partial \zeta}\frac{\partial \zeta}{\partial z}\right)\right\}\frac{\partial \zeta}{\partial z} = S_\Phi \tag{19}$$

3.2. Numerical scheme and solution procedure

For solving the governing equations with the finite difference method, the physical domain represented by a boundary-fitted coordinate system must be transformed into a rectangular domain, Discretization of equation (19) is performed by using the finite difference approximations in the transformed domain. The second order central differencing is used for approximating the diffusion terms, while the hybrid differencing scheme is employed for the convection terms.

The finite difference equation is arranged by collecting the terms according to the grid nodes around a control volume. Figure 2 illustrates the finite difference grid representation of the physical and transformed plane, respectively. The final expression is given by equation (20) in which A represents the link coefficients between grid nodes:

$$A_P\Phi_P = A_E\Phi_E + A_W\Phi_W + A_T\Phi_T + A_B\Phi_B + S_d \tag{20}$$

where

$$A_P = A_E + A_W + A_T + A_B + a_P^\circ$$

$$S_d = \int_V S_\Phi r|J|\,d\xi\,d\zeta + A_{TE}\Phi_{TE} + A_{BE}\Phi_{BE} + A_{TW}\Phi_{TW} + A_{BW}\Phi_{BW} + a_P^\circ\Phi_P^\circ + \frac{\rho\Delta H r_c(f_L - f_L^\circ)}{\Delta t}|J|$$

$$a_P^\circ = \frac{\rho r_c}{\Delta t}|J| \tag{21}$$

In the above equations the superscript $^\circ$ denotes the solution at the previous time level. Thus, the nonlinear equations of transportation are approximated by a system of linear algebraic equations. The governing equations used in the present analysis are nonlinear and strongly coupled. Iterative procedures are employed to derive a converged solution from the equations.

In the present study, the staggering grid systems were used. The velocity components, u and w, were solved and stored at the grid nodes and the pressure, p, was located at the corners of the control volume of u and w. The governing equations were represented in a finite difference form and solved iteratively on a line-by-line basis utilizing a Tri-Diagonal Matrix Algorithm (TDMA). The SIMPLE-C algorithm, employed for the details of the procedure, is described elsewhere [14].

Figure 3 represents the domain for analyzing the arc and weld pool. A mesh generation for a 120 A arc with 2 mm arc length is shown in Fig. 3(A), in which 40 nodes

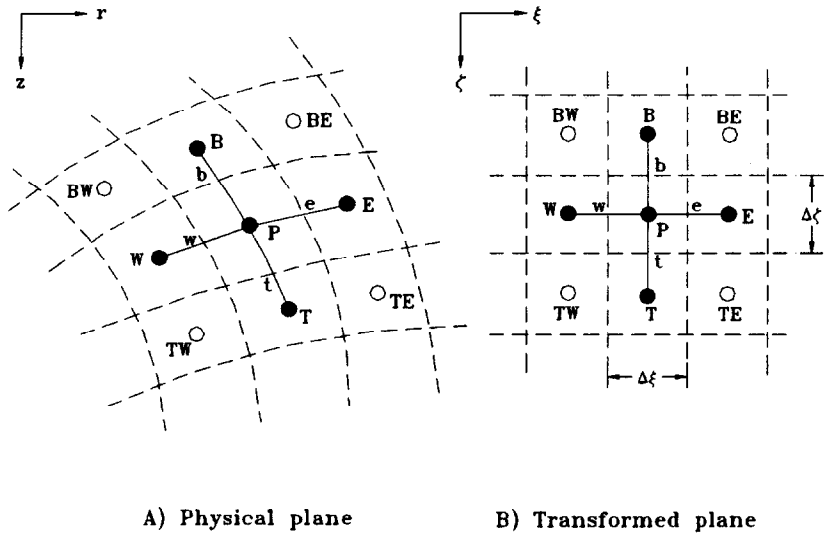

Fig. 2. Finite-difference grid representation.

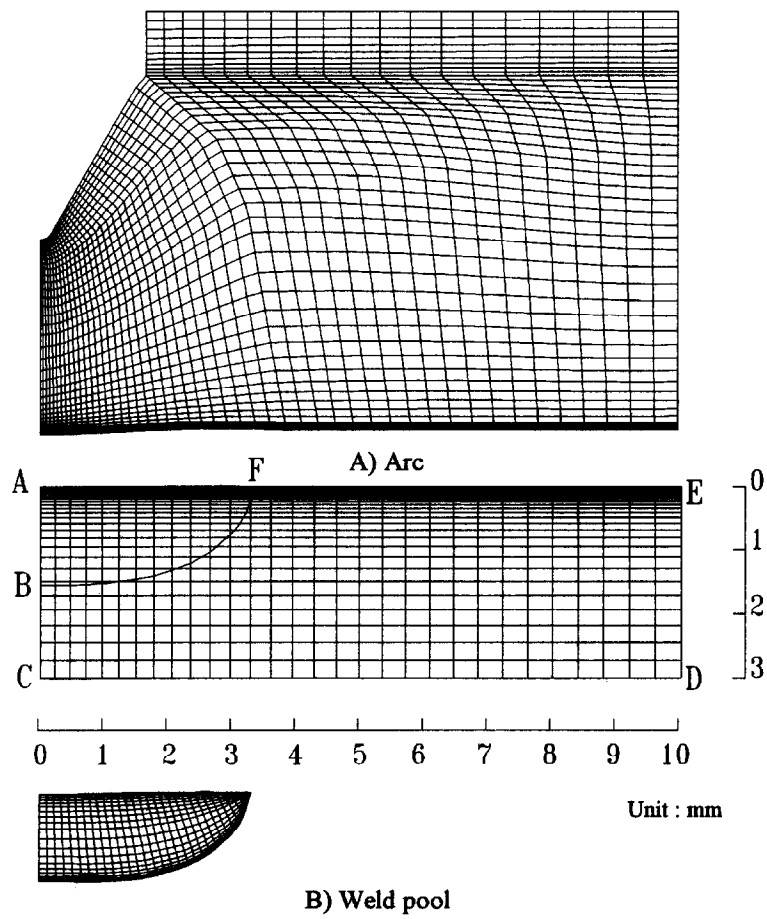

Fig. 3. Solution domain and mesh generation with boundary-fitted coordinates.

in the r-direction and 60 nodes in the z-direction are located in the arc domain. The boundary-fitted nodes are generated in order to describe the cathode shape and the free surface at the anode. The finer mesh is used near the cathode and the anode. Figure 3(B) represents two different domains. Region ACDE is for analyzing the electrical potential and temperature distribution, region ABF is represented boundary-fitted nodes for analyzing the conservation of momentum because the fluid flow takes place only within the fusion boundary. Therefore, recalculating the fusion region for the momentum equation is necessary whenever one time step elapsed. The calculated dependent variables in region ACDE must also transform to region ABF, or vice versa, every time step. The plate considered for the analysis has a radius of 10.0 mm (r-direction) and a thickness of 3.0 mm (z-direction). The heat source is assumed to be located at the center of the plate. Due to the axisymmetry with respect to the center plane, the calculations were done only for one side of the plane. The model used a 31×30 variable rectangular grid system for calculations. In order to improve the accuracy of calculations, a grid system of variable spacing was used, i.e., finer spacing near the heat source and coarser grid away from the center. The minimum radial grid was 0.23 mm, while the minimum axial grid was 0.006 mm.

Numerical calculations were performed for the AISI 304 stainless steel plate containing 10 ppm sulfur. Table 2 lists the physical properties for AISI 304 stainless steel taken from several sources [1, 7, 9, 11, 15]. The temperature-dependent thermal conductivity and specific heat used in the calculations are shown in Fig. 4. The time step is 0.002 s and the calculation is terminated after the lapse of 2.0 s of real time.

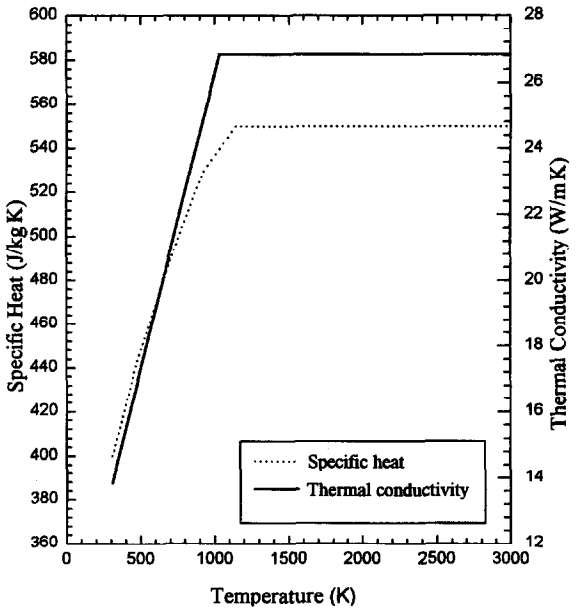

Fig. 4. Thermal conductivity and specific heat of AISI 304 stainless steel.

The iterative procedure for the calculation of velocity and temperature distribution was continued until the following convergence criterion was satisfied:

$$\frac{\sum_{i=1}^{L}\sum_{k=1}^{N}\left|\Phi_{i,k}-\Phi_{i,k}^{\text{old}}\right|_{\text{m}}}{\Phi_{\max}} < \varepsilon_{\Phi},\ \varepsilon_{\Phi} = 0.01 \tag{22}$$

Table 2
Material properties of AISI 304 stainless steel

Nomenclature	Symbol	Unit	Value
Activity of sulfur	a_i	wt%	0.001
Constant in surface tension gradient	A_γ	N (m K)$^{-1}$	1.0×10^{-4}
Density	ρ	kg m^{-3}	7200.0
Effective viscosity	μ	kg (m s)$^{-1}$	0.05
Electrical conductivity	σ	Ω^{-1} m^{-1}	7.7×10^5
Emissivity of body surface	ε	—	0.9
Gas constant	R_g	J (kg mole K)$^{-1}$	8314.3
Latent heat of fusion	ΔH	J kg^{-1}	2.47×10^5
Liquidus temperature	T_L	K	1723
Magnetic permeability of vacuum	μ_0	H m^{-1}	1.26×10^{-6}
Solidus temperature	T_S	K	1673
Specific heat	C_p	J (kg K)$^{-1}$	Fig. 4
Standard heat of adsorption	ΔHo	J (kg mole)$^{-1}$	-1.88×10^8
Surface excess at saturation	Γ_s	J (kg mole m^2)$^{-1}$	1.3×10^{-8}
Surface tension a pure metal	γ_m	N m^{-1}	1.943
Thermal conductivity	k	W (m K)$^{-1}$	Fig. 4

4. Process variables

Figure 5 is a schematic representation of an ideal pulsed current rectangular wave form showing the associated pulse parameters. For this wave form, characteristic measures defining the current are as follows:

(1) The mean current, I_M, which represents the same electric effect as a constant current of this value:

$$I_M = \frac{1}{t_T}\int_0^{t_T} I dt = \frac{(I_P \times t_P)+(I_B \times t_B)}{(t_P + t_B)}$$

$$= \frac{(I_P \times t_P)+(I_B \times t_B)}{t_T}; \quad (23)$$

(2) The effective current or root mean square current, I_E, which represents the same thermal effect as a constant current of this value:

$$I_E = \left(\frac{1}{t_T}\int_0^{t_T} I^2\, dt\right)^{\frac{1}{2}} = \left(\frac{I_P^2 \cdot t_P + I_B^2 \cdot t_B}{t_T}\right)^{\frac{1}{2}}; \quad (24)$$

(3) The current ratio, $r_E = I_B/I_P$, of the background current, I_B, to the peak pulse current, I_P;

(4) The peak to total time ratio, $r_I = t_P/t_T$, of the peak pulse duration, t_P, to the total pulse cycle, $t_T = t_P + t_B$;

(5) The pulse time ratio, $t_R = t_P/t_B$, of the peak pulse duration, t_P, to the background pulse duration, t_B;

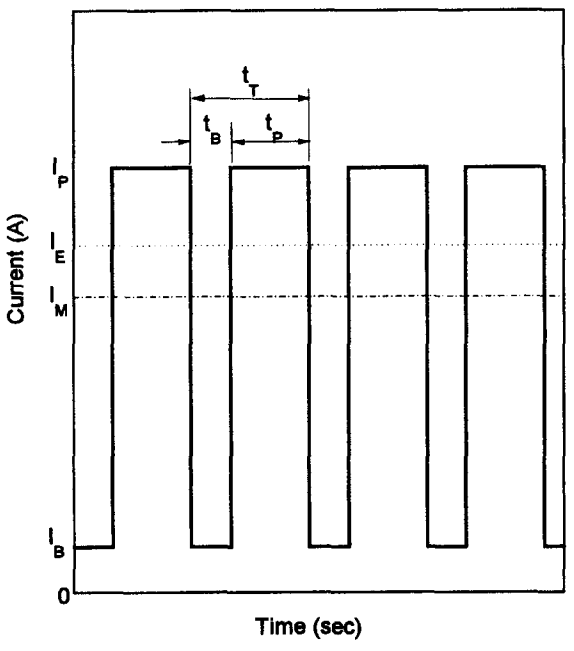

Fig. 5. Schematic of an ideal pulsed current square wave form and associated pulse parameters.

(6) The pulse cycle frequency, $F_P = 1/(t_P + t_B) = 1/t_T$, the reciprocal of the cycle time, t_T;

(7) The relationship between I_M and I_E:

$$\frac{I_M}{I_E} = \frac{r_I + r_E(1-r_I)}{\{r_I + r_E^2(1-r_I)\}^{1/2}}. \quad (25)$$

I_M is therefore always a little lower than I_E and the difference of I_E and I_M $(I_E - I_M)$ is greater than the lower values of r_E and r_I. For pulsed current GTA welding, the values r_E and r_I are generally greater than 0.3 [13]. The parameters of pulsed current GTA welding used for computations are shown in Table 3, while Fig. 6 represents a typical arrangement of the pulse time ratio used in this investigation for an effective current of 100 A. All of the non-pulse process parameters were held constant through the investigation and represented in Table 4. The pulse parameters were evaluated in terms of their influence on the weld pool shape, bead depth, penetration, surface velocity and temperature distribution.

5. Results and discussion

Transporting phenomena into the anode plate such as heat flux, current density, anode gas shear stress and arc pressure were obtained from the results of Lee et al. [16] and Kim et al. [17]. The characteristics of the calculated welding arc results for each current at 2.0 mm arc length are shown in Fig. 7. These are the typical boundary conditions for the weld pool model.

The variation of weld pool depth, half width and aspect ratio (depth to half-width ratio of the weld pool) as a function of time is shown in Fig. 8 for three cases of Table 3. The solid continuous line in this figure is the result calculated for an effective current of 100 A for comparison. As can be seen in this figure, the weld pool width represents a very clear change at each peak and background current. The width and depth of weld pool increases steeply during the peak current period. During the background current period, the weld pool width decreases, while the weld pool depth decreases or increases only slightly. As the ratio t_P/t_B increases, the weld pool width decreases, while the depth of penetration slightly increases. Consequently the decrease in t_P/t_B resulted in a wider weld bead with no distinct enhancement in depth of penetration. Similar observations were reported by Leither et al. [2], Omar et al. [18] and Jackson et al. [19]. The increase in weld bead width at high peak current is probably due to the arc expansion (radial arc growth) which causes an impingement of arc plasma on a wider area of the weld specimen.

Figures 9 and 10 represent the stream lines and velocity fields in various weld pool calculated for three different pulse time ratios at the welding time of 1.5 and 1.92 s, respectively. The welding time of 1.5 s is corresponding

Table 3
Parameters for pulsed current GTA welding

Parameters	Notation	Case 1	Case 2	Case 3
Background current, A	I_B	36	40	48
Background duration, s	t_B	0.16	0.24	0.32
Current ratio	r_E	0.3	0.3	0.3
Effective current, A	I_E	100	100	100
Mean current, A	I_M	92	88	85
Peak pulse current, A	I_P	120	136	160
Peak pulse duration, s	t_P	0.32	0.24	0.16
Peak to total time ratio	r_t	0.67	0.50	0.33
Pulse cycle frequency, Hz	F_P	2.08	2.08	2.08
Pulse time ratio (t_P/t_B)	t_R	2.0	1.0	0.5
Relationship between I_M and I_E		0.92	0.88	0.85
Remarks		Fig. 6(A)	Fig. 6(B)	Fig. 6(C)

Table 4
Non-pulse welding parameters

Welding parameter	Unit	Value used
Arc length	mm	2.0
Arc voltage	V	14.0
Electrode angle	deg	60
Electrode diameter	mm	3.2
Electrode tip diameter	mm	0.4
Electrode type	—	2% thoriated tungsten
Nozzle diameter	mm	12.7
Shielding gas (Ar)	$l\,min^{-1}$	10.0

to the background current period, while 1.92 s to the peak current period. It also represents the case of 100 A effective current for comparison. All the flow patterns show a similar trend, that is, the molten liquid in the surface flows radially outward from the middle of the pool surface to the solid-liquid interface. This may be due to the negative value of surface tension gradient with respect to temperature because of a low level of 10 ppm sulfur content. As the welding time increases, the maximum velocity in the weld pool also increases. The calculated velocities of the liquid metal agree qualitatively well with the results of previous theoretical investigations.

Figure 11 represents the iso-thermal lines for various pulse time ratios at the welding time of 2.0 s. The iso-thermal lines in three cases are from the liquidus temperature (1450°C) to 350°C with a constant interval of 100°C. The characteristics of penetration depth and bead width are similar to those of Figs. 9 and 10. As can be seen from this figure, the appropriate pulse parameters of the GTA welding process where maximum penetration and minimum bead width are achieved include the high t_P and low t_B value.

Figures 12 and 13 show the surface velocity profiles as the function of radial position calculated for the considered three cases at the welding time of 1.5 and 2.0 s, respectively. All the surface velocity profiles show a similar trend, that is, in general the surface velocity is radially outward except at the solid-liquid interface, where it is radially inward. For 'Case 3' at the welding time of 1.92 s, the surface velocity is always radially outward.

Figure 14 shows the surface velocity profiles as the function of radial position calculated for various time steps of 'Case 1'. The solid continuous line in this figure represents the results at the peak current value and the dotted line the result at the background current value. All the surface flow patterns show a similar trend, in which at peak current level the velocity is higher than at the background current level.

Figure 15 shows the surface temperature profiles as the function of radial position calculated for various time steps of 'Case 1'. The solid continuous line in this figure represents the result at the peak current value and the dotted line that of the background current value. It can be found that the surface temperature during the peak

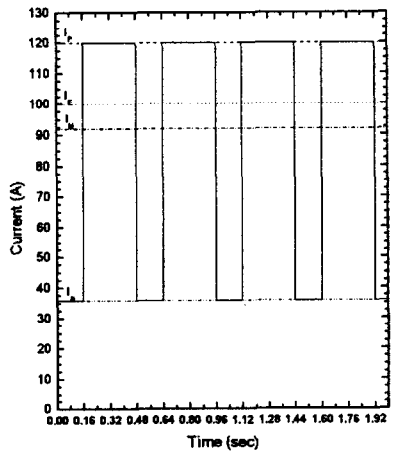

A) Case 1 ($t_R = 2.0$)

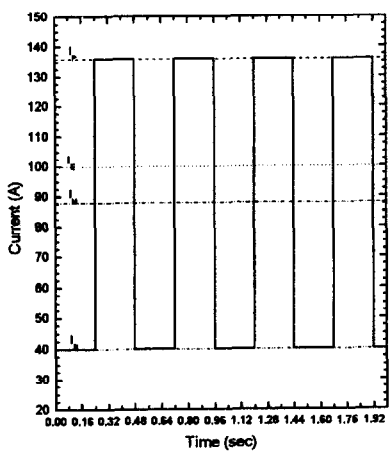

B) Case 2 ($t_R = 1.0$)

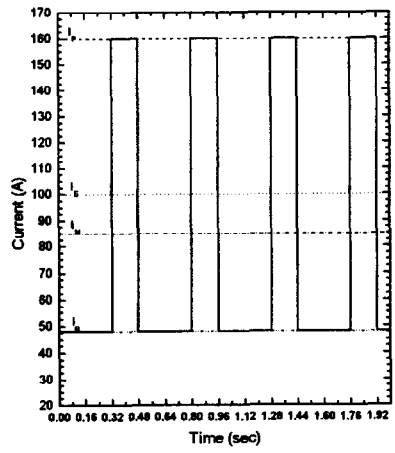

C) Case 3 ($t_R = 0.5$)

Fig. 6. Typical examples of pulse time ratio t_R and associated parameters.

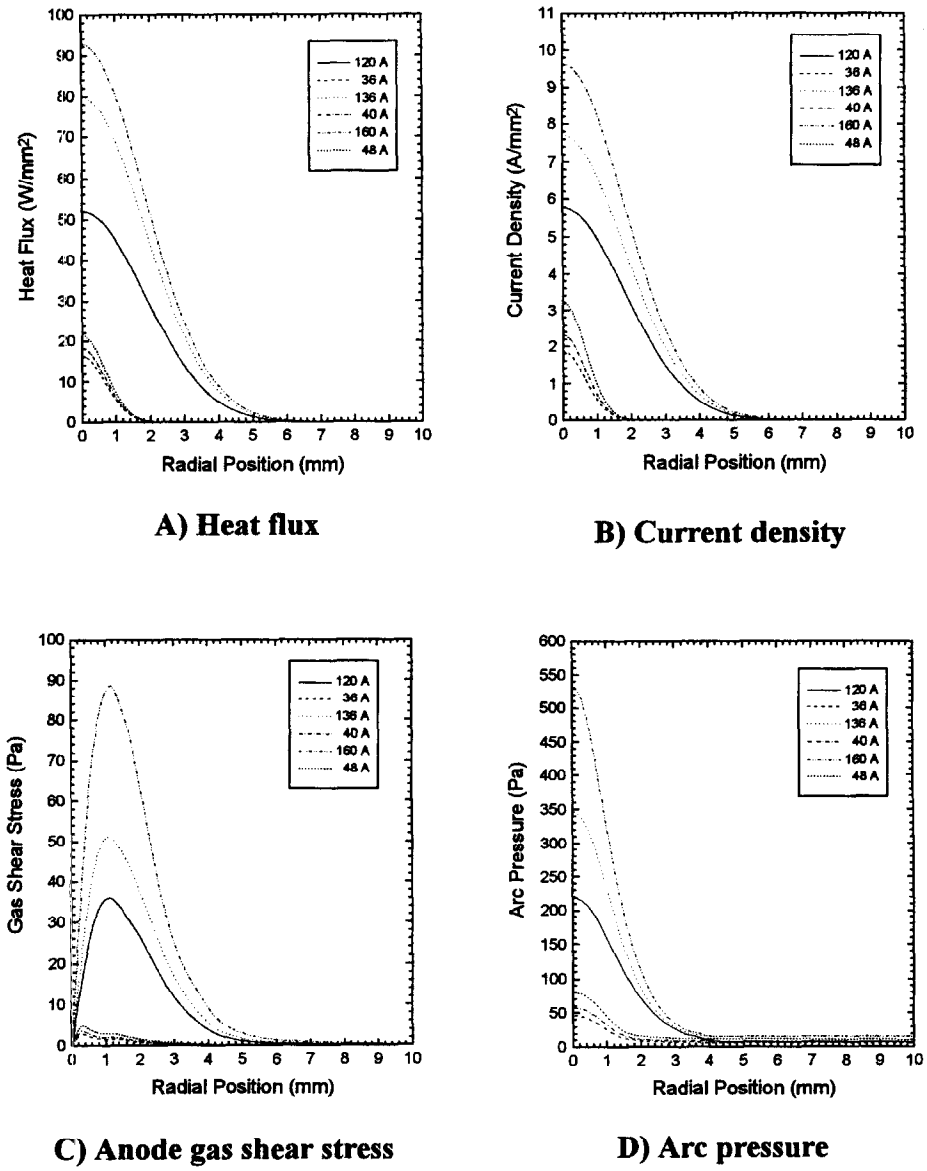

Fig. 7. Arc characteristics on weld pool surface.

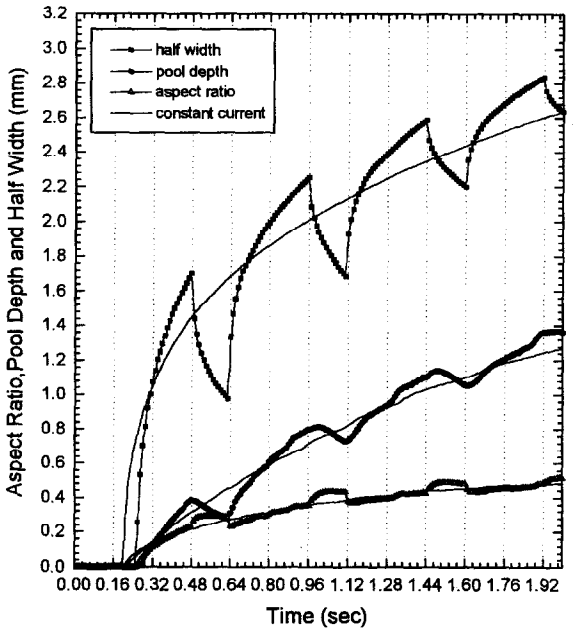

A) Case 1

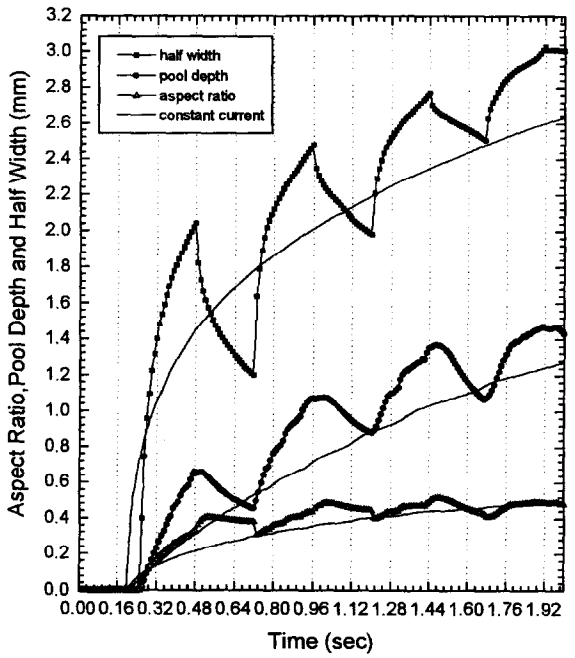

B) Case 2

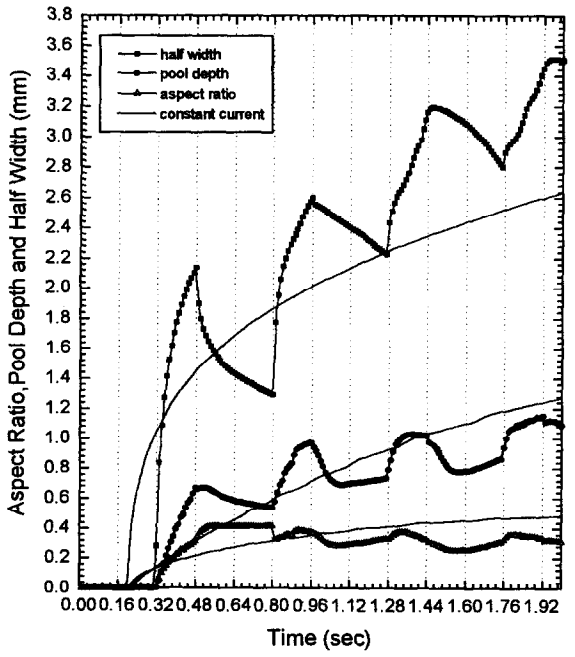

C) Case 3

Fig. 8. Aspect ratio, pool depth and half width calculated for various pulse time ratios.

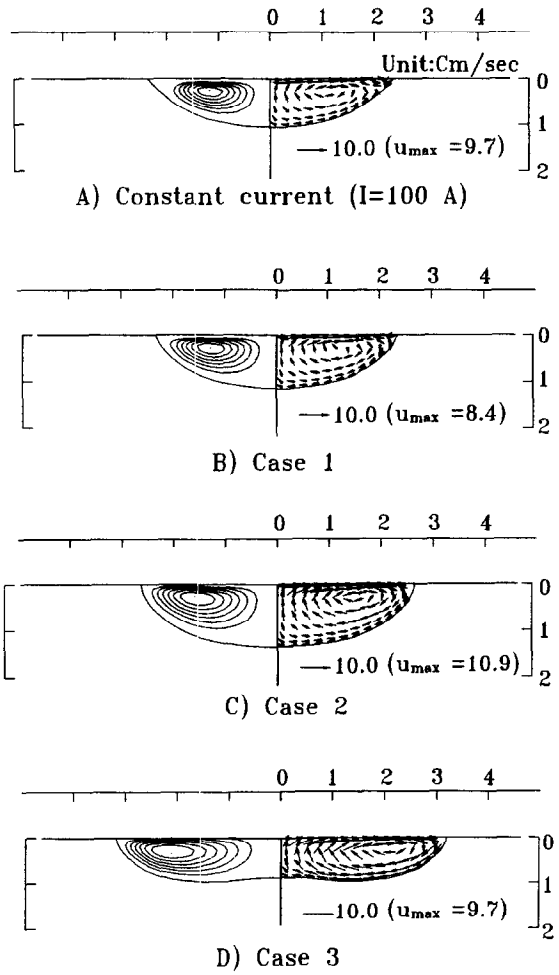

Fig. 9. Weld pool characteristics calculated for various pulse time ratios at welding time of 1.5 s.

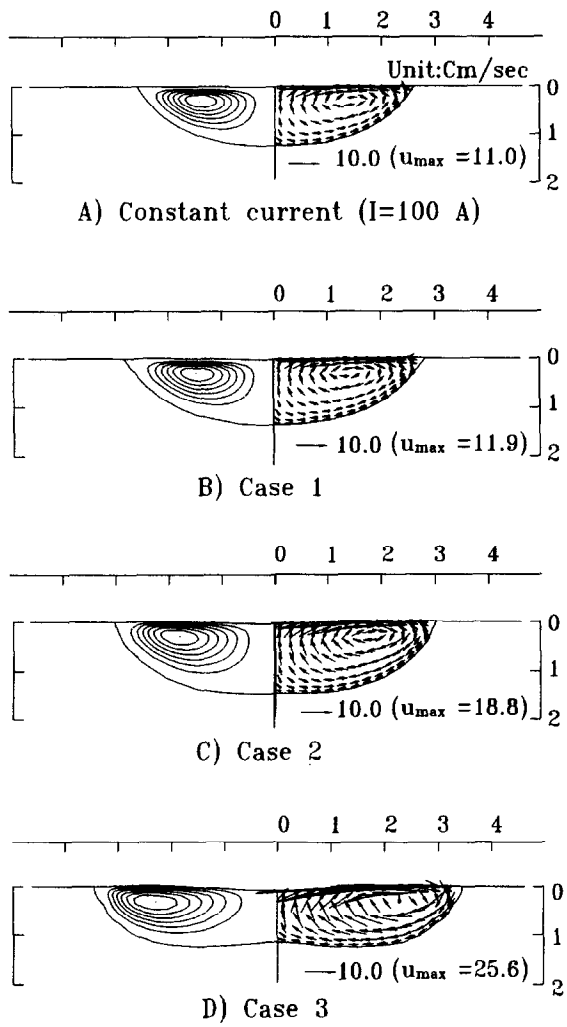

Fig. 10. Weld pool characteristics calculated for various pulse time ratios at welding time of 1.92 s.

current period is higher than that during the background current period, especially when the surface temperature is above the material liquidus temperature.

6. Conclusions

The governing equations for transient, two-dimensional heat and fluid flow problems associated with the pulsed current GTA welding process were solved to ascertain the behavior of weld pool. The transporting phenomena from the welding arc to the base material surface were derived from the simulation results of the corresponding welding arc, and the effect of surface depression due to the arc pressure acting on the weld pool surface was considered. A boundary-fitted coordinate system was adopted to precisely describe the curved and unknown fusion boundary.

Major conclusions observed in this study may be summarized as follows:

1. A numerical analysis can be performed for the phenomena of heat and fluid flow problems in the pulsed current GTA welding process. This heat and fluid flow model offers a useful means of predicting the complex behavior of weld pool in pulsed current GTA welding.
2. The increase of pulse time ratio (t_P/t_B) resulted in a deeper penetration for the same effective current and other settings.
3. No marked advantage is observed when the low pulse time ratio operation is utilized, that is, the lower the pulse time ratio, the wider the weld bead and the shallower the weld penetration.

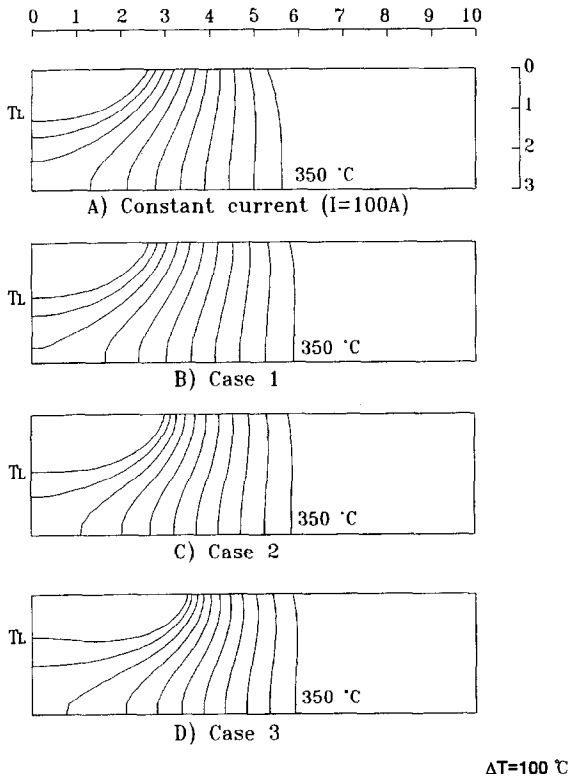

Fig. 11. Iso-thermal lines calculated for various pulse time ratios at welding time of 2.0 s.

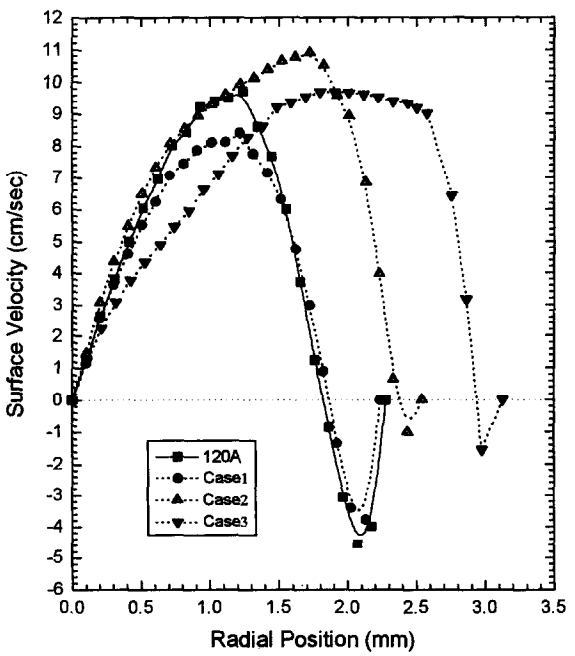

Fig. 12. Surface velocity calculated for various pulse time ratios at welding time of 1.5 s.

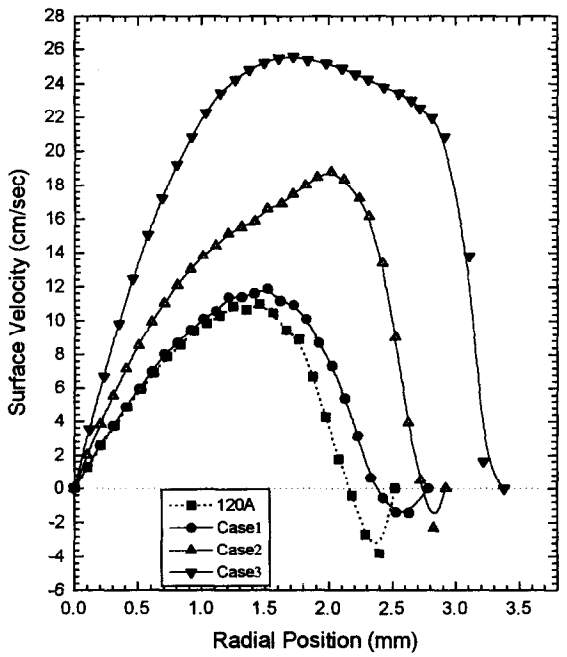

Fig. 13. Surface velocity calculated for various pulse time ratios at welding time of 1.92 s.

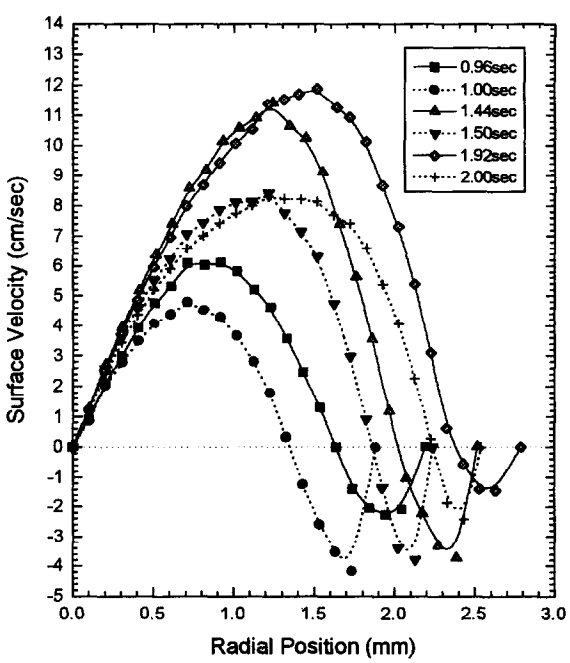

Fig. 14. Surface velocity calculated for various time steps of 'Case 1'.

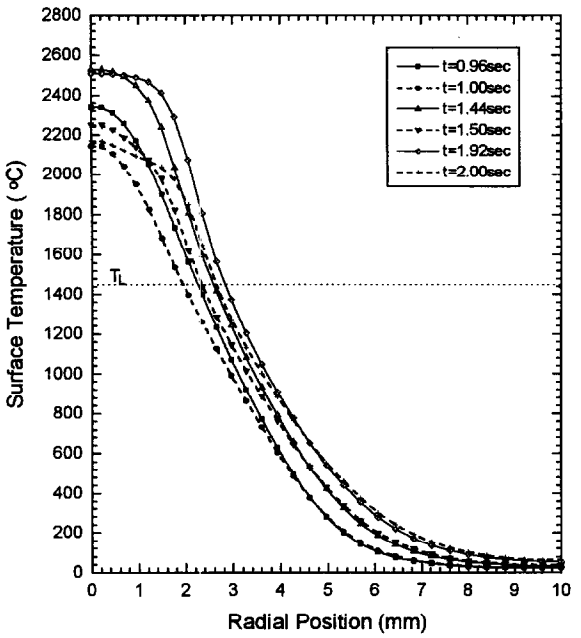

Fig. 15. Surface temperature calculated for various pulse time steps of 'Case 1'.

References

[1] Thompson ME, Szekely J. The transient behavior of weld pools with a deformed free surface. Int. J. Heat Mass Transfer 1989;32(6):1007–1019.

[2] Leitner RE, McElhinney GH, Pruitt EL. An investigation of pulsed GTA welding variables. Weld. J., Res. Suppl. 1973:405s–410s.

[3] Saedi HR, Unkel W. Arc weld pool behavior for pulsed current GTAW. Weld. J., Res. Suppl. Nov. 1988:247s–255s.

[4] Vishnu PR, Li WB, Easterling KE. Heat fluid model for pulsed welding. Materials Science and Technology 1991;7:649–659.

[5] Kanouff M, Greif R. The unsteady development of a GTA weld pool. Int. J. Heat Mass Transfer 1992;35(4):967–979.

[6] Choo RTC, Szekely J. The effect of gas shear stress on Marangoni flows in arc welding. Weld. J., Res. Suppl. 1991;233s–233s.

[7] Choo RTC, Szekely J, Westhoff RC. Modeling of high-current arcs with emphasis on free surface phenomena in the weld pool. Weld. J., Res. Suppl. 1990;346s–361s.

[8] Sahoo P, Debroy T, McNallan MT. Surface tension of binary metal surface active solute systems under conditions relevant to welding metallurgy. Metall. Trans. B 1988;19B,:483–491.

[9] Zacharia T, David SA, Vitek JM, Debroy T. Weld pool development during GTA and laser beam welding of type 304 stainless steel, Part I—Theoretical analysis. Weld. J., Res. Suppl. 1989;499s–509s.

[10] Goldak J, Bibby M, Moore J, Patel B. Computer modeling of heat flow in welds. Metall. Trans. 1986;17B:587–600.

[11] Touloukian YS. Thermophysical properties of high temperature solid materials, Vol. 3, The Macmillan Co., 1967.

[12] Ohji T, Nishiguchi K. Mathematical modeling of molten pool in arc welding of thin plate, IIW Doc. 211-555-83, 1988.

[13] Cornu J. Advanced Welding Systems, Vol. 3, Tig and related process, IFS(Publications) Ltd, U.K., 1988, pp. 59–77.

[14] Patankar SV. Numerical heat transfer and fluid flow, McGraw-Hill, 1980.

[15] Choo RTC, Szekely J, Westhoff RC. On the calculation of the free surface temperature of gas-tungsten-arc weld pools from first principles: Part I. Modeling the welding arc. Metall. Trans. B 1992;23B:357–369.

[16] Lee SY, Na SJ. A numerical analysis of a stationary gas tungsten welding arc considering various electrode angle. Weld. J., Res. Suppl. 1996;269s–279s.

[17] Kim WH, Fan HG, Na SJ, A mathematical model of gas tungsten arc welding considering the cathode and the free surface. Metall. Trans. 1997;28B:679–686.

[18] Omar AA, Lundin CD. Pulsed plasma—pulsed TGA arc: a study of the process variables. Weld. J., Res. Suppl. Apr. 1979;97s–105s.

[19] Jackson CE, Niles RW. Weld thermal efficiency of the GTAW process. Weld. J., Res. Suppl 1975;25s–32s.